METALLOPORPHYRIN STRUCTURE AND DYNAMICS FROM RESONANCE RAMAN SPECTROSCOPY

THOMAS G. SPIRO, ROMAN S. CZERNUSZEWICZ and XIAO-YUAN LI

Department of Chemistry, Princeton University, Princeton, NJ (U.S.A.)

(Received 4 April 1989)

CONTENTS

A. INTRODUCTION

The resonance Raman (RR) spectra of metalloporphyrins have inspired intense research activity over the past 15 years [1]. Biochemical interest has inspired much of this work, and indeed the first metalloporphyrin spectra were obtained for heme proteins [2,3]. These studies revealed novel spectroscopic phenomena which were of considerable theoretical interest. Structured excitation profiles were discovered and some RR bands were found to have anomalous polarization [4], a phenomenon that Placzek had predicted some 40 years earlier in a footnote to his well-known monograph on Raman theory [5]. This prediction had been overlooked, however, and the existence of vibrational Raman bands with higher intensity in perpendicular than in parallel polarization, which contravened the polarization rules cited in textbooks, came as a genuine surprise to spectroscopists.

In addition to these novel characteristics, which reflect the nature of the porphyrin excited states, the early heme protein studies revealed ground state vibrational frequency shifts associated with the ligation chemistry of the heme group [6–8]. Subsequent work has uncovered useful structure–spectra correlations, including sensitivities of specific band fre-

quencies to the porphyrin core size [9–11], and to the ligation, oxidation and spin state of the central metal ion [1(c)].

In addition, most of the RR bands have been assigned to metalloporphyrin normal modes on the basis of extensive isotope substitution studies and normal-coordinate analyses [12–16]. A valence force field has recently been developed that gives a good account of frequencies and isotope shifts for nickel porphyrins with different peripheral substituents [17,18]. These advances make it possible to apply RR spectroscopy in a discriminating way to interesting aspects of metalloporphyrin structural dynamics. This article reviews recent developments in this field from the authors' laboratory.

B. ELECTRONIC STRUCTURE AND RR ENHANCEMENT

Porphyrins are aromatic macrocycles with four pyrrole rings connected by unsaturated methine bridges at the four corners of a square (Fig. 1). The extended π system gives rise to a relatively small HOMO–LUMO energy gap (ca. 2 eV), and consequently metalloporphyrins absorb light strongly in the visible region of the spectrum. Figure 2 shows the absorption spectrum of ferrocytochrome c [19], which illustrates the classical features of metalloporphyrin spectra: a very intense B (or Soret) band near 400 nm, and a pair of weaker bands, Q_0 and Q_1 (or α and β), between 500 and 600 nm. Figure 2 also illustrates Gouterman's four-orbital model [20], on the basis of which these bands are readily understood. The LUMO is a degenerate π^* pair, of e_g symmetry (in the idealized D_{4h} point group), while the two HOMOs are a_{1u} and a_{2u}, and have nearly the same energy. Consequently, there is a large interaction between the two lowest energy orbital excitations (both of E_u symmetry). The transition dipoles add up for the intense B transition and nearly cancel for the weaker Q_0 transition (the intensity of which vanishes completely if a_{1u} and a_{2u} are accidentally degenerate). Some intensity
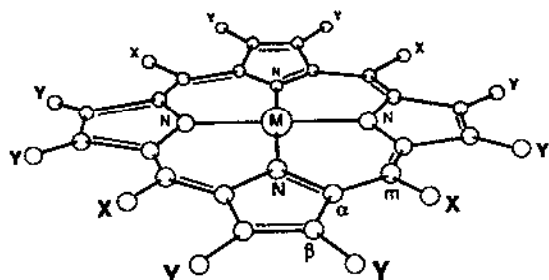

Fig. 1. Structural diagram of a D_{4h} metalloporphyrin with generalized peripheral substituents X and Y. The atom labelling scheme ($C_{\alpha,\beta,m}$) is shown.
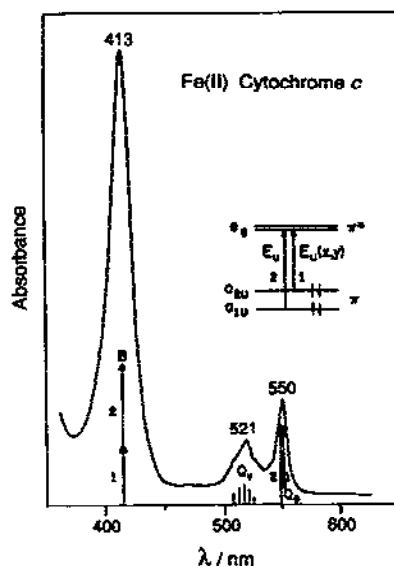
Fig. 2. Absorption spectrum of Fe(II) cytochrome c, with a schematic representation of the four-orbital model for the visible bands. The two $\pi - \pi$ orbital excitations, 1 and 2, are subject to strong configuration interaction, with the transition dipoles adding in the higher energy B transition, and nearly cancelling in the lower energy Q_0 transition. The Q_v band is the envelope of $0 \rightarrow 1$ vibronic transitions induced by mixing of the Q and B electronic transitions. (From ref. 19.)

(about 10%) is regained for the Q transition via vibronic mixing with the B transition, producing the Q_v sideband, which is the envelope of vibrational bands built on the Q_0 band.

RR spectra of metalloporphyrins display a wealth of peaks, arising from the vibrational modes of the porphyrin ring and of the peripheral substituents, the relative intensities of which depend dramatically on the laser excitation frequency. This is illustrated in Fig. 3 which shows survey spectra of NiOEP (OEP = octaethylporphyrin) at three excitation wavelengths. Near resonance with the B absorption band (406.7 nm excitation, top) the spectra are dominated by polarized peaks arising from totally symmetric vibrations. (The depolarization ratio, $\rho = I_{\perp}/I_{\parallel}$, is close to the expected value, 1/8, for resonance with in-plane electronic transitions in D_{4h} symmetry [21].) This dominance reflects the fact that only totally symmetric vibrations, those along whose coordinates the excited state potential surface is shifted, are subject to the main enhancement mechanism (Franck–Condon or "A term") for allowed electronic transitions [21]. Also seen with moderate intensity are some depolarized bands ($\rho = 3/4$, see for example ν_{10}), which are believed to be activated by a Jahn–Teller effect in the degenerate excited state [22].
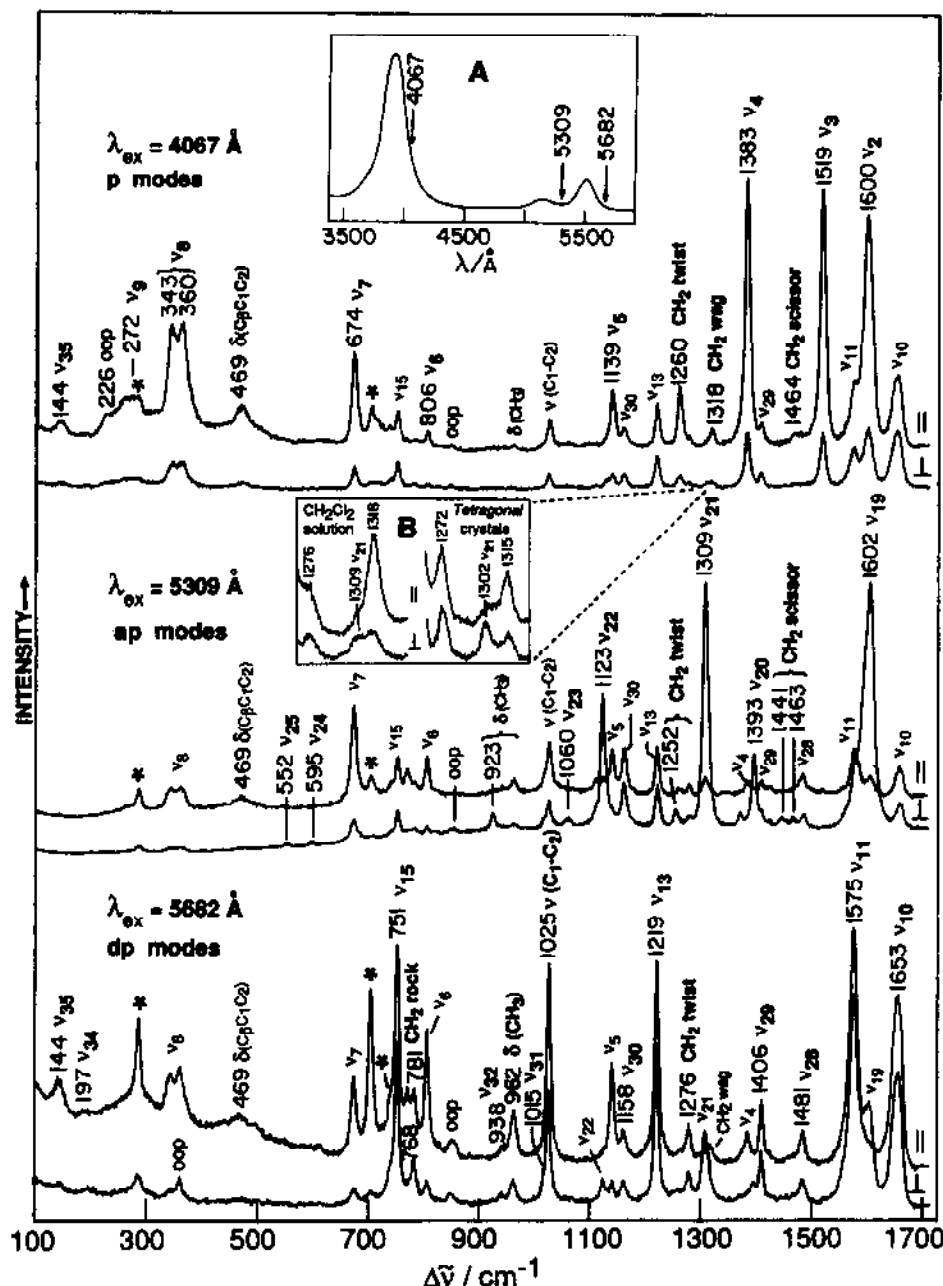
Fig. 3. RR spectra in parallel ($\parallel$) and perpendicular ($\perp$) scattering, of NiOEP (ca. 1 mM) in CH$_2$Cl$_2$, at the three indicated excitations, which bring out selectively the A_{1g}(p) 4067 Å, A_{2g}(ap) (5309 Å), and B_{1g}, B_{2g}(dp) (5682 Å) modes, the assignments of which are given by the labels (oop = out-of-plane). Solvent bands are indicated with asterisks. Conditions: backscattering from spinning NMR tube; 150 mW laser power; 3 cm^{-1} slitwidths; one scan, 1 s integration time at 0.5 cm^{-1} increments. Insets: (A) UV–visible spectrum of NiOEP in CH$_2$Cl$_2$ (arrows indicate excitation wavelengths used for RR measurements); (B) exploded view of the 1250–1350 cm^{-1} region of RR spectra of NiOEP in CH$_2$Cl$_2$ solution and tetragonal crystals showing enhancement of the ν_{21} (A_{2g}) skeletal mode with B-band

When the laser is near resonance (530.9 and 568.2 nm) with the Q absorption bands, RR peaks which are depolarized (dp) or anomalously polarized (ap, $\rho > 3/4$) become dominant. These arise from non-totally symmetric modes, B_{1g} or B_{2g} and A_{2g} respectively, which are effective in mixing the Q and B transitions (and which also give rise to the Q_v absorption band). They are enhanced via the non-Franck–Condon or "B term" mechanism [21] which is particularly effective for weak transitions that gain intensity from vibronic mixing. The enhancement is subject to an interference effect among the 0–0 and 0–1 vibronic transitions which selects for A_{2g} modes at wavelengths between these transitions and B_{1g} or B_{2g} modes at shorter or longer wavelengths [21]. This is the reason why ap bands are dominant with 530.9 nm excitation, while dp bands are dominant with 568.2 nm excitation (Fig. 3).

Since the Q_0 band, though much weaker than the B band, does have appreciable absorption strength (Fig. 3 inset), polarized peaks of moderate intensity can be seen in the Q-resonant spectra. However, their relative intensities differ dramatically from those of the B-resonant spectra. Thus RR peaks arising from the ν_2, ν_3 and ν_4 modes dominate the 406.7 nm excited spectrum, while the strongest polarized peaks in the 568.2 nm excited spectrum arise from ν_5, ν_6 and ν_7. This difference implies substantially different shapes for the B and Q excited state potentials [18].

Vibronic activity is also expected in the B-resonant RR spectra (due to the $Q-B$ mixing) but is quantitatively much less important than Franck–Condon activity because of the very large B absorption strength. The inset B of Fig. 3 shows that ap bands (which are activated vibronically but not via the Jahn–Teller effect, in contrast with the dp bands which can be activated by both mechanisms) can be detected at high magnification in B-resonant spectra.

The mode selectivity afforded by wavelength tuning is extremely useful in sorting out the numerous overlapping metalloporphyrin vibrational modes, especially when combined with isotope substitution. Figure 4 illustrates how five modes which are crowded into a 16 cm^{-1} region of the NiTPP (TPP = tetraphenylporphyrin) RR spectrum can be disentangled in this way.

C. IN-PLANE SKELETAL MODES

Through variable-wavelength RR spectroscopy and multiple isotope substitution it has been possible to assign essentially all of the Raman active in-plane skeletal modes of the nickel complexes of porphine [17], TPP [17] and OEP [16,18]. Most IR-active modes have also been assigned for the first [17] and last [23] of these complexes. Nickel was chosen as the central metal for these studies because it forms stable, easy-to-purify, four-coordinate
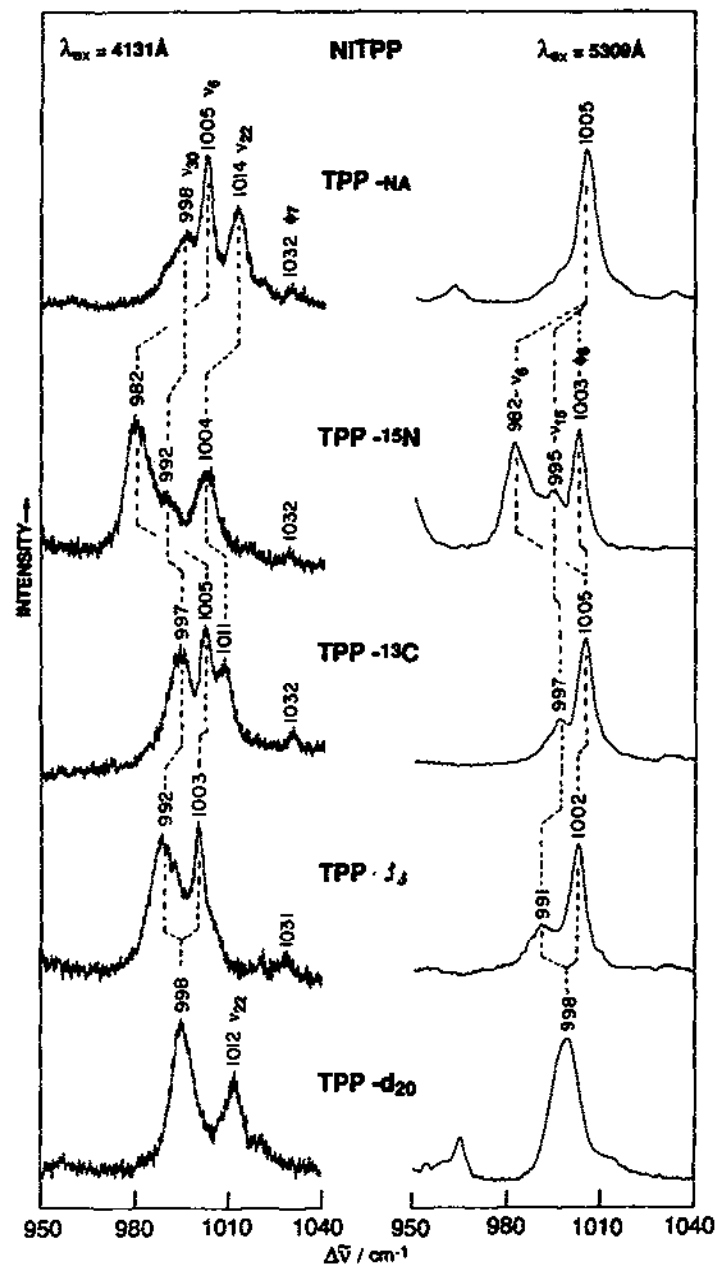
Fig. 4. Details of the 950–1050 cm^{-1} RR spectra of NiTPP in CS$_2$ with 4131 Å (left panel) and 5309 Å (right panel) excitation. (From ref. 17.)

metalloporphyrins which do not fluoresce. The three porphyrins were chosen in order to vary the substitution pattern systematically (Fig. 1) from unsubstituted (X = Y = H) to *meso*-substituted (X = phenyl, Y = H) to pyrrole-

substituted (X = H, Y = ethyl), while maintaining four-fold symmetry. In this way the influence of substituents on the skeletal modes could be assessed systematically.

In cataloguing the porphyrin skeletal modes, the substituents X and Y are counted as point masses. The 37-atom D_{4h} model has 71 in-plane modes, which classify as

$$\Gamma_{\text{in-plane}} = 9A_{1g} + 8A_{2g} + 9B_{1g} + 9B_{2g} + 18E_u$$

The E_u modes are IR active, while the remaining modes are Raman active. The skeletal mode assignments for the three nickel porphyrins are listed in Table 1. These assignments are supported by normal-coordinate calculations of the frequencies and isotope shifts [17,18] and are quite secure. The calculations included the TPP phenyl groups fully, while the OEP ethyl groups were included as methylene groups with point mass methyl substituents. The final force constants were in general accord with those which have been reported for simpler aromatic molecules, and the bond stretching force constants scaled with bond distance in a manner consistent with the results of ab initio calculations [17]. A minimum set of interaction force constants was included, the 1,2 and 1,3 stretch–stretch interactions having alternating signs as expected for aromatic systems. The frequencies of all three metalloporphyrins were successfully reproduced with only slight force constant variations, reflecting the slight electronic differences introduced by the different substituents [17,18].

The local coordinate which is the main contributor to each of the modes is given in Table 1. A pictorial illustration of these coordinates is given in Fig. 5. They are bond stretchings and bendings in their symmetric and antisymmetric combinations, or cooperative motions of the pyrrole rings (half- or quarter-ring bond stretches, breathing, deformation, rotation and translation). It can be seen from Table 1 that modes with the same local mode designation in different symmetry blocks have quite similar frequencies. The differences that do exist result from the different patterns of mode mixing within the blocks. The mode designations, ν_i, stem from the assignment of the NiOEP spectrum by Kitagawa and coworkers [16], who numbered the modes in order of descending frequency in the A_{1g} block followed consecutively by the B_{1g}, A_{2g}, B_{2g} and E_u blocks. In order to keep the mode numbering for corresponding modes of all three porphyrins, the strict frequency order had to be abandoned for porphine and TPP because of the very different frequencies for C–X and C–Y stretching and bending modes when a hydrogen atom is replaced by a phenyl or ethyl substituent [17].

In general, there is a fairly close frequency correspondence among the three porphyrins, with the obvious exception of modes which involve the substituent (or hydrogen) atoms directly. Indirect effects of the altered

TABLE 1

In-plane skeletal mode frequencies (cm^{-1}) and local mode assignments for nickel(II) complexes of OEP, porphine and TPP [a] (from ref. 18)

Symmetry	ν_i	Description [b]	NiOEP	NiP	NiTPP
A_{1g}	ν_1	$\nu(C_m-X)$	(3041) [c]	(3042)	1235
	ν_2	$\nu(C_\beta-C_\beta)$	1602	1575	1572
	ν_3	$\nu(C_\alpha-C_m)_{sym}$	1520	1459	1470
	ν_4	ν(Pyr. half-ring)$_{sym}$	1383	1376	1374
	ν_5	$\nu(C_\beta-Y)_{sym}$	1138	(3097)	(3097)
	ν_6	ν(Pyr. breathing)	804	995	1004
	ν_7	δ(Pyr. def.)$_{sym}$	674	731	889
	ν_8	ν(Ni–N)	360/343	369	402
	ν_9	$\delta(C_\beta-Y)_{sym}$	263/274	1066	1079
B_{1g}	ν_{10}	$\nu(C_\alpha-C_m)_{asym}$	1655	1650	1594
	ν_{11}	$\nu(C_\beta-C_\beta)$	1577	1505	1504
	ν_{12}	ν(Pyr. half-ring)$_{sym}$	1331 [d]	1319 [d]	1302
	ν_{13}	$\delta(C_m-X)$	1220	1185	238
	ν_{14}	$\nu(C_\beta-Y)_{sym}$	1131	(3079)	(3097)
	ν_{15}	ν(Pyr. breathing)	751	1003	1009
	ν_{16}	δ(Pyr. def.)$_{sym}$	746 [c]	730	846
	ν_{17}	$\delta(C_b-Y)_{sym}$	305	1060	1084
	ν_{18}	ν(Ni–N)	168	237	277
A_{2g}	ν_{19}	$\nu(C_\alpha-C_m)_{asym}$	1603	1611	1550
	ν_{20}	ν(Pyr. quater-ring)	1394	1354	1341
	ν_{21}	$\delta(C_m-X)$	1307	1139	(257)
	ν_{22}	ν(Pyr. half-ring)$_{asym}$	1121	1005	1016
	ν_{23}	$\nu(C_\beta-Y)_{asym}$	1058	(3087)	(3087)
	ν_{24}	δ(Pyr. def.)$_{asym}$	597	806	828
	ν_{25}	δ(Pyr. rot.)	551	429	560
	ν_{26}	$\delta(C_\beta-Y)_{asym}$	(243)	1317	1230
B_{2g}	ν_{27}	$\nu(C_m-X)$	(3041)	(3041)	1269
	ν_{28}	$\nu(C_\alpha-C_m)_{sym}$	1483	1504	(1481)
	ν_{29}	ν(Pyr. quarter-ring)	1407	1368	1377
	ν_{30}	ν(Pyr. half-ring)$_{asym}$	1160	1003	1004
	ν_{31}	$\nu(C_\beta-Y)_{asym}$	1015	(3088)	(3087)
	ν_{32}	δ(Pyr. def.)$_{asym}$	938	819	869
	ν_{33}	δ(Pyr. rot.)	493	435	450
	ν_{34}	$\delta(C_\beta-Y)_{asym}$	197	1193	1191
	ν_{35}	δ(Pyr. transl.)	144	197	109
E_u	ν_{36}	$\nu(C_m-X)$	(3040)	(3042)	(1254)
	ν_{37}	$\nu(C_\alpha-C_m)_{asym}$	(1637)	1624	(1586)
	ν_{38}	$\nu(C_\beta-C_\beta)$	1604	1547	(1552)
	ν_{39}	$\nu(C_\alpha-C_m)_{sym}$	1501	1462	(1473)
	ν_{40}	ν(Pyr. quarter-ring)	1396	1385	(1403)
	ν_{41}	ν(Pyr. half-ring)$_{sym}$	(1346)	1319	(1331)

TABLE 1 (continued)

Symmetry	ν_i	Description[b]	NiOEP	NiP	NiTPP
E_u	ν_{42}	$\delta(C_m-X)$	1231	1150	(233)
	ν_{43}	$\nu(C_\beta-Y)_{sym}$	1153	(3097)	(3097)
	ν_{44}	$\nu(Pyr.\ half\text{-}ring)_{asym}$	1133	1033	(1003)
	ν_{45}	$\nu(C_\beta-Y)_{asym}$	996	(3087)	(3100)
	ν_{46}	$\delta(pyr.)_{asym}$	927	806	(864)
	ν_{47}	$\nu(Pyr.\ breathing)$	766[d]	995	(1023)
	ν_{48}	$\delta(pyr.)_{sym}$	605	745	(895)
	ν_{49}	$\delta(Pyr.\ rot.)$	544	366	(512)
	ν_{50}	$\nu(Ni-N)$	(358)	420	(436)
	ν_{51}	$\delta(C_b-Y)_{asym}$	328[e]	1064	(1093)
	ν_{52}	$\delta(C_\beta-Y)_{sym}$	263[e]	1250	(1213)
	ν_{53}	$\delta(Pyr.\ transl.)$	212[e]	282	(306)

[a] A and B mode frequencies from CS_2 solution (NiOEP, NiP) and crystal (NiTPP) RR spectra at room temperature. E mode frequencies from matrix-isolated (NiOEP) [23] and room temperature KBr pellet (NiP) IR spectra.
[b] Local coordinates descriptions in Fig. 5. X, Y = H, H(NiP); H, C_2H_5 (NiOEP) and C_6H_5, H (NiTPP).
[c] ( ), calculated frequencies; not observed.
[d] Observed only in the $meso\text{-}d_4$ isotopomers.
[e] These frequencies from 12 K RR spectra of tetragonal crystals [34].

substituents can largely be traced to the altered couplings of the skeletal modes. Thus the asymmetric $C_\alpha C_m$ stretching modes ν_{10} and ν_{19} are ca. 60 cm^{-1} lower in NiTPP than in NiP or NiOEP, mainly due to the loss of the $\delta(C_m H)$ interaction, unique to the B_{1g} and A_{2g} blocks, which pushes ν_{10} and ν_{19} up. However, the $C_\beta-C_\beta$ stretches, ν_2 and ν_{11}, are 50–70 cm^{-1} higher for NiOEP than NiP or NiTPP because of the altered interactions when a hydrogen atom is substituted by an ethyl group on the C_β atoms. Even larger interaction effects can be seen in the mid- and low-frequency regions. The pyrrole breathing modes, ν_6 and ν_{15}, are near 1000 cm^{-1} for NiP and NiTPP, close to the value for free pyrrole, but are lowered by 200–250 cm^{-1} in NiOEP via interaction with the ethyl groups. However, the symmetric pyrrole deformation modes, ν_7 and ν_{16}, are near 700 cm^{-1} for NiP and NiOEP, but are pushed up 100–120 cm^{-1} in NiTPP by interactions with a phenyl deformation mode [18].

The metal–N(pyrrole) stretching modes are of interest, since their assignment in heme proteins has been controversial [24]. For NiP and NiTPP the $B_{1g}(\nu_{18})$ Ni–N frequency is near 250 cm^{-1}, a frequency consistent with the large effective mass of the pyrrole rings. For comparison the breathing mode frequency of Cu(ImH)$_4^{2+}$ is 245 cm^{-1} [25]. The A_{1g} and E_u counterparts (ν_8 and ν_{50}) are at much higher frequencies, near 400 cm^{-1}. This elevation
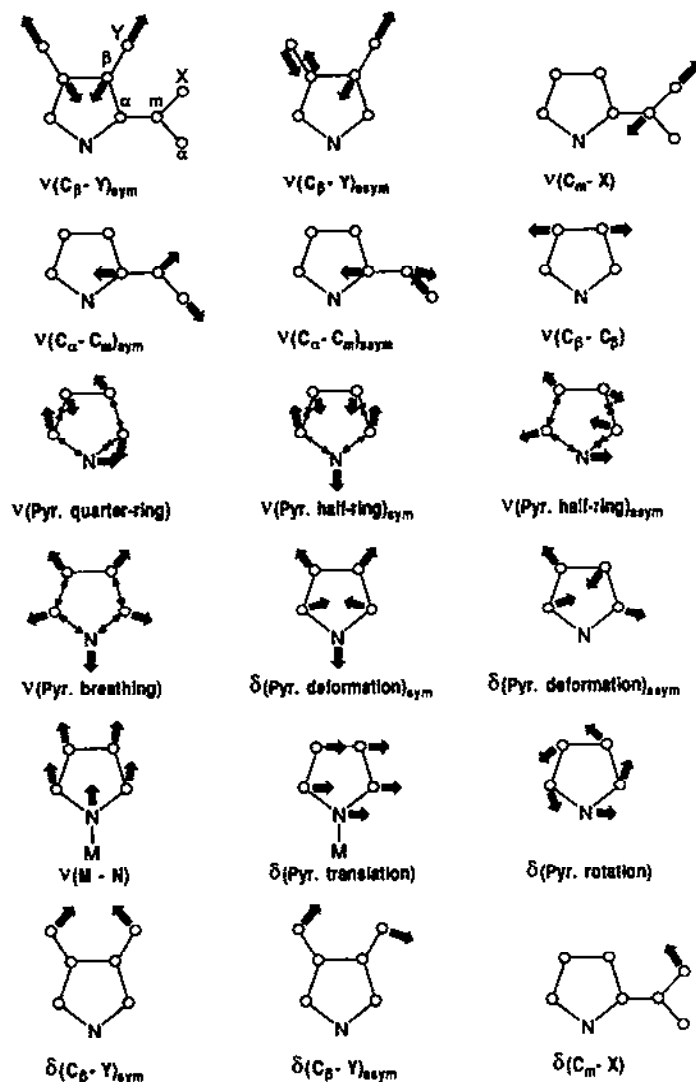
Fig. 5. Illustration of the local coordinates used in classifying the in-plane porphyrin skeletal modes. The stretching motions of the $C_\alpha N$ and $C_\alpha C_\beta$ pyrrole bonds are considered collectively, and classified according to the phases of the individual bonds shown by light arrows. (From ref. 17.)

reflects the fact that the $C_\alpha C_m C_\alpha$ angles must expand when adjacent Ni–pyrrole bonds are stretched in phase, but not when they are stretched out of phase. Consequently, the force constant for the mode contains $C_\alpha C_m C_\alpha$ bending as well as Ni–N stretching contributions for the A_{1g} and E_u modes, but not for the B_{1g} mode. The case of NiOEP is more complex because of

strong interactions between the Ni–N stretching modes, which involve translation of the pyrrole rings, and bending of the C_β–ethyl bonds. The result is a pair of bands in each of the symmetry blocks with substantial $\nu(Ni–N)/\delta(C_\beta–Y)_{sym}$ coordinate mixing. The situation is further complicated by a strong dependence of these modes on the mutual disposition of the ethyl groups (pointing up or down) on a given pyrrole ring [18]. The multiple orientations allowed in solution are believed to give rise to doublet structures of these bands, particularly noticeable in the case of ν_8 and ν_9. This interpretation of the strong ν_8 doublet at ca. 350 cm^{-1} replaces the previous assignment to a Fermi resonance between ν_8 and the overtone of ν_{35} [16]. In view of these complexities, it is not surprising that the role of metal–N(pyrrole) stretching in heme protein RR spectra has been elusive.

D. SUBSTITUENT MODES

In addition to the skeletal modes, a number of internal substituent modes have been identified in the RR spectra of both NiTPP and NiOEP via H/D substitution on the phenyl rings [17] and on the methylene carbon atom of the ethyl groups [18]. There are two ways in which substituent modes can gain enhancement in resonance with the porphyrin $\pi-\pi^*$ transitions: (1) the mode can mix with a skeletal mode and thereby borrow some of its enhancement; and (2) the mode can be enhanced directly, i.e. electronically, if it participates in the excited state distortion.

Inspection of the NiTPP spectra suggests that vibrational mixing accounts for most of the intensity of the phenyl modes [17]. For example, the highest frequency phenyl mode, ϕ_4, at 1599 cm^{-1}, is fairly prominent in B-resonant RR spectra, probably because it mixes with the nearby (1572 cm^{-1}) very strong ν_2 mode. This mixing is demonstrated by the 4 cm^{-1} upshift of ν_2 when the phenyl groups are perdeuterated, as the interaction is relieved by a large ϕ_4 downshift. The calculated eigenvectors of these modes are compared in Fig. 6. The ν_2 mode is mainly pyrrole $C_\beta–C_\beta$ stretching in character, but significant phenyl involvement can be seen. Conversely, the phenyl mode shows appreciable $C_\beta–C_\beta$ stretching, which could well account for its intensity, without any need to invoke an electronic role for the phenyl groups. The other phenyl modes which appear in the RR spectra likewise fall near skeletal modes with which they mix significantly [17]. Although there is a potential for electronic interaction between the phenyl and porphyrin π systems, this interaction is minimized by the orthogonal orientation of the rings. The steric contact between the hydrogen atoms on the pyrrole and phenyl rings produces a substantial barrier to phenyl rotation [26]. NMR data indicate minimal phenyl–porphyrin conjugation [27].
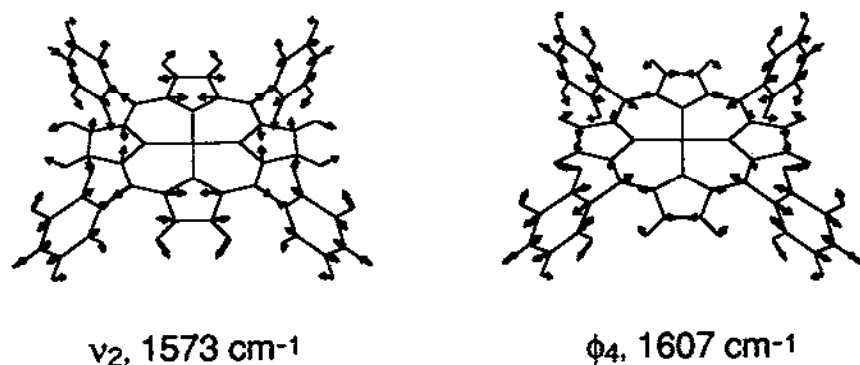
ν_2, 1573 cm⁻¹ ϕ_4, 1607 cm⁻¹

Fig. 6. Eigenvectors of ν_2 and the adjacent phenyl mode ϕ_4, showing coordinate mixing. (From ref. 17.)

Surprisingly, enhancement of ethyl modes in the NiOEP RR spectra cannot be explained by vibrational coupling alone. The clearest example is provided by the peak at 1025 cm⁻¹ that shows up at all excitation wavelengths (Fig. 2). This peak is identified with the ethyl groups by its large shift upon methylene deuteration [18]. Ethyl modes are calculated at this frequency in all the symmetry blocks; they mainly (ca. 65%) involve stretching of the (outer) ethyl C1C2 bond, mixed with $C_\beta C1$ stretching (which itself gives rise to the strong ν_5 peak) [18]. While the 1025 cm⁻¹ peak is A_1 in character in the B-resonant spectra, both A_1 and B_1 contributions are evident in the Q-resonant spectra, since an intermediate depolarization ratio is seen. (The isotope shift pattern also distinguishes the A_1 and B_1 modes [18].) With 568.2 nm excitation, the 1025 cm⁻¹ peak is the strongest in the spectrum and it has substantial intensity at 406.7 nm as well. It is therefore evident that localized ethyl modes are directly enhanced by both A- and B-term mechanisms, and that the ethyl group must somehow be coupled electronically to the porphyrin $\pi-\pi^*$ transitions.

Electronic coupling is readily understood when the substituent is conjugated with the porphyrin, as in protoporphyrin, whose conjugated vinyl groups give rise to a number of vinyl RR bands [28], or in heme a, which has conjugated vinyl and formyl groups [29–31]. The formyl C=O stretch produces a prominent band in heme a RR spectra, and formyl conjugation is readily evident even in the ground state since $\nu(C=O)$ is sensitive to the heme electronic structure; it shifts down about 20 cm⁻¹ between high and low spin iron(II) complexes due to $d\pi-\pi^*$ back-donation in the latter [31]. The enhancement of ethyl modes for NiOEP is unexpected and implies that electronic coupling need not involve conjugation of unsaturated bonds. We have suggested [18] that hyperconjugation [32(a)] might account for the ethyl mode intensities. As illustrated in Fig. 7, when the ethyl group is oriented

(a)   **(b)**

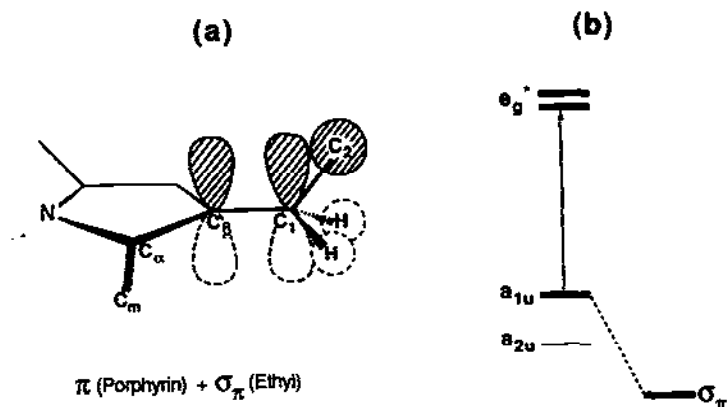π (Porphyrin) + σ_π (Ethyl)

Fig. 7. Diagram of hyperconjugative interaction in OEP which is proposed to account for ethyl mode RR enhancements. The out-of-plane ethyl orientation optimizes the orbital alignment (a). The ethyl σ_π–porphyrin a_{1u} interaction (b) modulates the electronic transition energy and induces excited state origin shifts and vibronic couplings along ethyl coordinates. (From ref. 18.)

with the $C_\beta C1C2$ plane orthogonal to the porphyrin plane (the sterically favored orientation), the filled σ_π orbital can interact with the a_{1u} HOMO (which has significant electron density on the C_β atoms), thereby raising its energy and lowering the π–π^* transition energy. Internal motions of the ethyl group, especially stretching of the C–C bonds, would modulate this interaction and thereby distort the excited state, leading to resonance enhancement.

E. OUT-OF-PLANE MODES

The 37-atom D_{4h} model predicts 34 out-of-plane (oop) metalloporphyrin modes, which classify as

$$\Gamma_{oop} = 3A_{1u} + 6A_{2u} + 5B_{1u} + 4B_{2u} + 8E_g$$

They are expected at relatively low frequencies. C–H oop modes occur between 1100 and 800 cm^{-1}, while the remaining modes are at lower frequencies. Only the E_g modes are Raman active, and, being non-totally symmetric, they require vibronic activity for enhancement. They are unable, however, to mix the in-plane π–π^* transitions, which are of E_u symmetry, since $E_u \times E_u (= A_{1g} + A_{2g} + B_{1g} + B_{2g})$ does not contain the E_g representation. They are only able to mix in-plane with out-of-plane (A_{2u}) transitions: $E_u \times A_{2u} = E_g$. Thus within the four-orbital model there can be no RR enhancement of any oop mode. The porphyrin ring itself has no A_{2u}

electronic transitions at accessible wavelengths, but one might be provided by a porphyrin $(a_{2u}) \rightarrow$ metal $d_z^2(a_{1g})$ charge transfer transition. A weak z-polarized absorption at 450 nm has been observed and assigned to this transition in oriented-crystal spectra of several low spin iron(II) heme proteins [32(b)]. It is possible that this transition, mixing with the nearby B transition, may be responsible for the appearance of the 841 cm^{-1} C–H oop band in 457.9 nm excited RR spectrum of aqueous $(ImH)_2Fe(II)PP$ (ImH = imidazole, PP = protoporphyrin) [33].
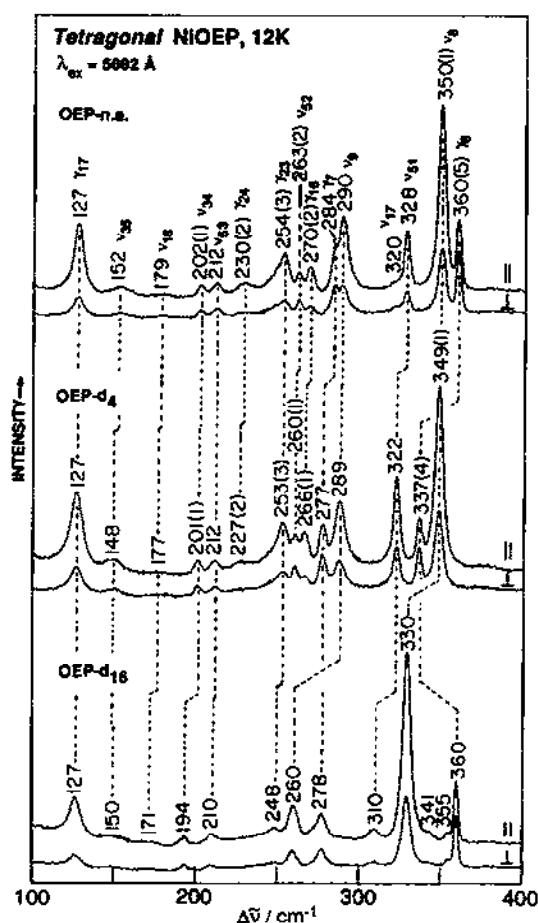

Fig. 8. Excited (5682 Å) low temperature (12 K) RR spectra (100–400 cm^{-1}) of tetragonal NiOEP and its *meso-d$_4$* and methylene-d_{16} isotopomers in KCl pellets. ^{15}N shifts are given in parentheses. Band assignments are indicated by the labels; in-plane modes are n_i while out-of-plane modes are γ_i. Conditions: 150 mW laser power; 3 cm^{-1} slitwidth; single scan; 0.5 cm^{-1} increments; 1 s integration time. (From ref. 34.)

In general, however, activation of oop modes requires symmetry lowering so that the selection rules are relaxed. Deviations from planarity of the porphyrin ring itself should be particularly effective in allowing oop modes to couple with the $\pi-\pi^*$ transitions. Such deviations are common in heme proteins, as judged from the available crystal structures, and heme protein RR spectra are often rich in low frequency bands, some of which may well arise from oop modes. In the absence of external constraints, metalloporphyrins prefer to have planar rings, so the oop data base has been very sparse [33].

Recently, however, we have been able to assign a majority of the NiOEP oop modes from RR spectra of tetragonal crystals [34], in which the porphyrin ring is known to be highly ruffled [35]. This distortion imposes symmetry lowering to the S_4 point group, in which the B_{1u} and B_{2u} modes transform as A, while the A_{1u} and A_{2u} modes transform as B, and the E_g modes transform as E. These are the same symmetry classes to which the in-plane modes are transformed, and the oop modes are therefore subject to $\pi-\pi^*$ enhancement via the A- or B-term mechanisms. Figure 8 illustrates the assignment of oop peaks (labelled γ_i) via their polarization properties and isotope shifts. The assignments, which are listed in Table 2, were supported by a normal-mode calculation, using oop force constants transferred from other aromatic molecules [34]. Because the calculation was carried out for a planar porphyrin, while the data are from a ruffled one, no attempt was made to refine the force field, and there are significant differences between some of the observed and calculated frequencies. Nevertheless, the correspondences in frequencies and isotope shifts are good enough to lend considerable confidence in the assignments. Also listed in Table 2 are mode descriptions in terms of local motions which are illustrated in Fig. 9. The ethyl internal coordinates were included in the calculation and the $C_\beta C1C2$ bend (δ) was found to mix importantly with the skeletal oop modes, especially those involving pyrrole folding, and to give rise themselves to several detectable RR bands. These are included in Table 2, which has eight additional entries for the eight δ coordinates.

Among the oop modes, $\gamma_6(A_{2u})$ at 360 cm^{-1} is of particular interest. In this mode the four pyrrole rings tilt in the same direction, producing a net doming of the porphyrin ring. A significant motion of the central metal results, as is revealed by a substantial $^{62/58}$Ni isotope shift, shown in Fig. 10. This mode is expected to play a role in the dynamics of ligand dissociation from six-coordinate metalloporphyrins; it has been shown to interact strongly with the asymmetric ImH–Fe–ImH stretching mode in $[(ImH)_2Fe(III)OEP]^+$ [36]. The IR spectrum of this complex reveals two bands which together split the expected ^{2}H isotope effects of γ_6 and the ligand stretch almost equally.

TABLE 2

Calculated and observed frequencies and ^{15}N isotopic shifts (cm^{-1}) for out-of-plane modes of NiOEP and its *meso-d$_4$* isotopomer [a] (from ref. 23)

| Mode	NiOEP ($\Delta^{15}N$)		NiOEP-d_4 ($\Delta^{15}N$)		Description [b]
	Obs.	Calc.	Obs.	Calc.	
A_{1u} (B) modes [c]					
γ_1	750 (0) [d]	725 (0)	749 (0)	725 (0)	Pyr. fold$_{asym}$
δ_1	445 (0)	474 (0)	444 (0)	474 (0)	$\delta(C_\beta C1C2)_{asym}$
γ_2	–	346 (0)	–	346 (0)	Pyr. swivel
γ_3	–	74 (0)	–	74 (0)	$\gamma(C_\beta C1)_{asym}$
A_{2u} (B) modes					
γ_4	844 (0)	829 (1)	681 (3) [e]	667 (6)	$\gamma(C_m H)$
γ_5	739 (6)	736 (6)	760 (2) [d]	763 (1)	Pyr. fold$_{sym}$
δ_2	525 (0)	562 (1)	524 (0)	561 (1)	$\delta(C_\beta C1C2)_{sym}$
γ_6	360 (5)	351 (5)	337 (4)	310 (4)	Pyr. tilt
γ_7	284 (0)	263 (1)	277 (0)	256 (0)	$\gamma(C_\alpha C_m)$
γ_8	–	108 (0)	–	107 (0)	$\gamma(C_\beta C1)_{sym}$
γ_9	–	32 (0)	–	32 (0)	$\gamma(NiN)$
B_{1u} (A) modes					
γ_{10}	853 (0) [f]	845 (0)	–	501 (0)	$\gamma(C_m H)$
γ_{11}	732 (0)	733 (0)	–	790 (0)	Pyr. fold$_{asym}$
γ_{12}	612 (0)	589 (0)	652 (0)	706 (0)	Pyr. swivel
δ_3	–	392 (0)	–	383 (0)	$\delta(C_\beta C1C2)_{asym}$
γ_{13}	–	130 (0)	–	125 (0)	$\gamma(C_\alpha C_m)$
γ_{14}	–	44 (0)	–	43 (0)	$\gamma(C_\beta C1)_{asym}$
B_{2u} (A) modes					
γ_{15}	704 (4)	627 (3)	702 (3)	627 (3)	Pyr. fold$_{sym}$
δ_4	477 (2)	538 (2)	477 (2)	538 (2)	$\delta(C_\beta C1C2)_{sym}$
γ_{16}	270 (2)	253 (3)	266 (1)	253 (4)	Pyr. tilt
γ_{17}	127 (0)	127 (1)	127 (0)	127 (1)	$\gamma(C_\beta C1)_{sym}$
γ_{18}	–	30 (0)	–	30 (0)	Pyr. transl.
E_g (E) modes					
γ_{19}	841 (0) [g]	836 (0)	–	773 (0)	$\gamma(C_m H)$
γ_{20}	–	731 (0)	–	712 (0)	Pyr. fold$_{asym}$
γ_{21}	656 (0) [h]	667 (3)	–	627 (3)	Pyr. fold$_{sym}$
δ_5	552 (3)/548 (0)	562 (0)	530 (1)	547 (2)	$\delta(C_\beta C1C2)_{sym}$
γ_{22}	494 (2) [g]	506 (1)	483 (1) [g]	484 (0)	Pyr. swivel
δ_6	–	382 (0)	–	371 (0)	$\delta(C_\beta C1C2)_{asym}$
γ_{23}	254 (3)	244 (3)	253 (3)	243 (2)	Pyr. tilt
γ_{24}	230 (2)	207 (1)	227 (2)	194 (1)	$\gamma(C_\alpha C_m)$
γ_{25}	–	91 (1)	–	91 (1)	$\gamma(C_\beta C1)_{sym}$
γ_{26}	–	63 (0)	–	63 (0)	$\gamma(C_\beta C1)_{asym}$
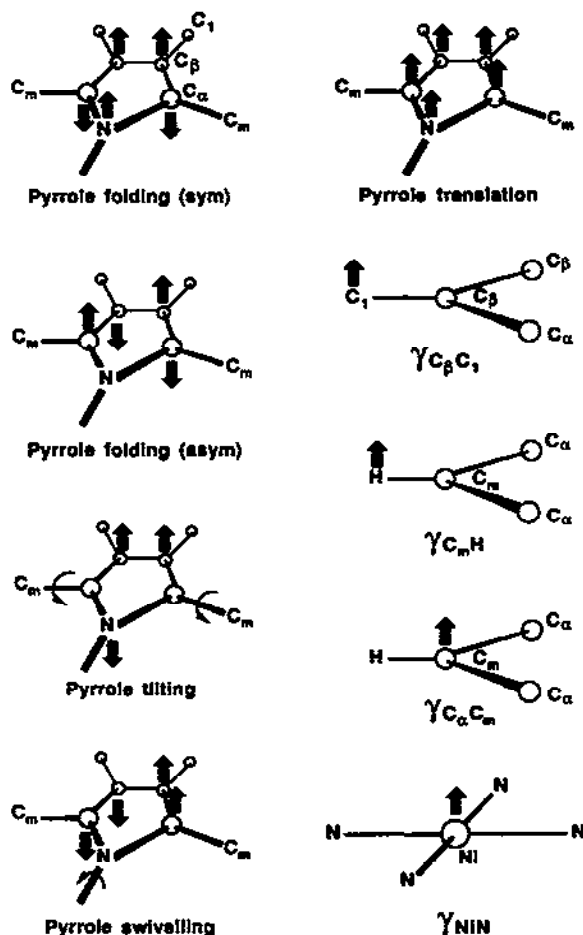
Fig. 9. Illustration of local modes used in the out-of-plane classification. Internal ethyl coordinates are not shown, but were included in the normal-coordinate calculation. (From ref. 34.)

Footnotes to Table 2:

[a] Observed values from RR spectra of tetragonal crystals at 12 K. Calculated methylene-d_{16} shifts are all zero, because of the orthogonality of the porphyrin and ethyl planes in the model [34]. Calculated $^{62/58}$Ni shifts are zero except for the four lowest A_{2u} (B) modes; 0.8, γ_6; 0.3, γ_7; 1.6, γ_8; and 0.8 cm^{-1}, γ_9.

[b] Mode descriptions (see Fig. 5) are based on the calculated eigenvectors [34]. Subscripts sym and asym indicate symmetric and asymmetric combinations with respect to the C_2' axis bisecting the pyrrole rings.

[c] Mode symmetry in the D_{4h} (S_4) point group.

[d] Overlapping bands.

[e] This value from KBr pellet IR spectrum at room temperature; in the RR spectrum this position is obscured by ν_{15}.

[f] Seen in solution RR spectra [39].

[g] These values from RR spectra of triclinic crystals at 12 K.

[h] Alternative assignment for this mode might be a weak 641 cm^{-1} dp band, which downshifts 3 cm^{-1} in the ^{15}N and meso-d_4 isotopomer spectra.
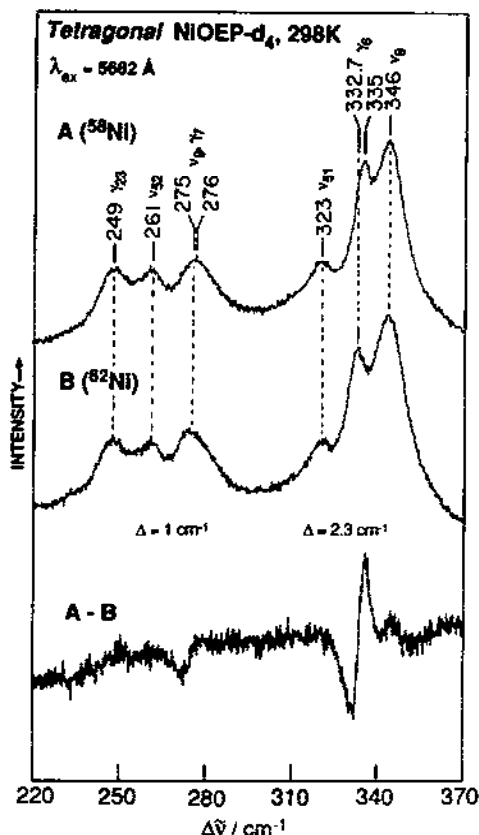
Fig. 10. Excited (5682 Å) room temperature RR spectra (220–370 cm^{-1}) of tetragonal NiOEP-d_4 (KCl) pellets with ^{58}Ni and ^{62}Ni. The difference spectrum shows the isotope shifts associated with the 335 and 276 cm^{-1} oop modes. Conditions: 150 mW laser power; 4 cm^{-1} slitwidth; 0.2 cm^{-1} increments; 2 s integration time. (From ref. 34.)

F. NiOEP RUFFLING DYNAMICS

The porphyrin ruffling in tetragonal NiOEP is attributable to the low spin Ni^{2+} ion being smaller than the standard porphyrin cavity size [37]. The pyrrole rings undergo a propeller twist (Fig. 11), which permits the Ni–N bonds to shorten by 0.02–0.03 Å relative to the flat structures found in triclinic crystals of NiOEP [38]. This strengthening of the Ni–N bonds is at the expense of the porphyrin π conjugation, which is maximized when the macrocycle is flat. The crystal polymorphism indicates that the planar and ruffled structures are nearly equal in energy, the form isolated depending on crystallization conditions. The question naturally arises where the balance of these forces lies in NiOEP solutions, when the molecules are unconstrained by packing forces.
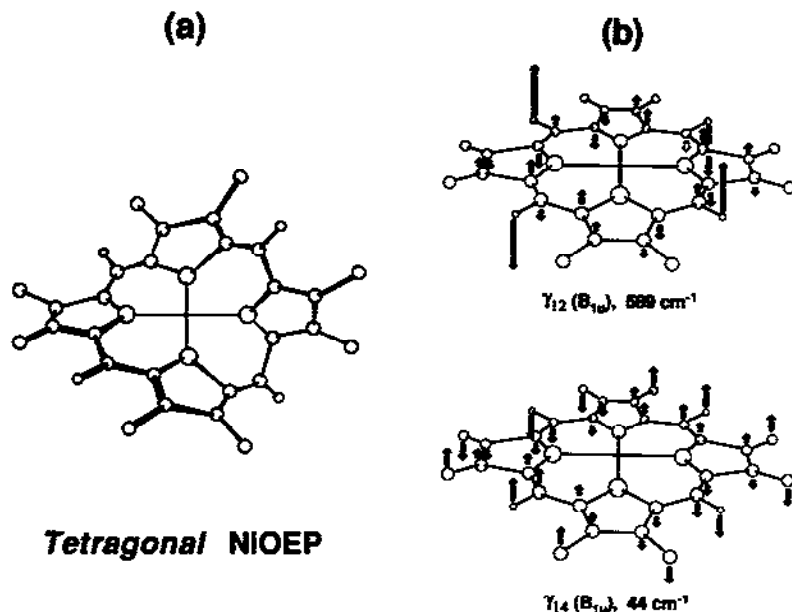
(a)　　　　　　　　　**(b)**

Tetragonal NiOEP

γ_{12} (B_{1u}), 589 cm^{-1}

γ_{14} (B_{1u}), 44 cm^{-1}

Fig. 11. Eigenvectors (b) of the B_{1u} modes, γ_{12} and γ_{14}, which can provide effective pathways for Ni–N bond shortening and porphyrin ruffling leading to the structure seen in tetragonal crystals (a). These modes are suggested to soften in solution. (From ref. 39.)

To answer this question, we examined the low frequency RR spectra of NiOEP solutions [39] and found definite evidence for the activation of the pyrrole tilting mode, γ_6, as shown in Fig. 12. Although the 350 cm^{-1} region is complicated by the doubling of the in-plane ν_8 mode, due to ethyl orientational isomerism, the band shape as a function of isotopic composition, particularly in the perpendicularly polarized spectrum, leaves no doubt that γ_6 is seen, and with an intensity comparable to that of the tetragonal crystal spectra. The depolarized character of this band shows that it results from the same symmetry lowering as in the tetragonal crystals, i.e. an S_4 distortion. Thus the NiOEP ring does ruffle in solution.

Other oop modes were also identified in the solution spectra, but one was conspicuously absent, namely the γ_{12} mode assigned to a fairly prominent polarized band in the tetragonal crystal spectra [34]. The eigenvector for this mode, illustrated in Fig. 11, shows it to be a propeller twisting motion of the pyrrole rings, a ruffling distortion. It was proposed [39] that this mode softened in solution, its potential curve flattened by the competing forces favoring a ruffled vs. a flat structure. The mode-softening mechanism is illustrated by the scheme suggested in Fig. 13, in which a potential favoring pyrrole twisting (linear for small displacements) is added to a harmonic
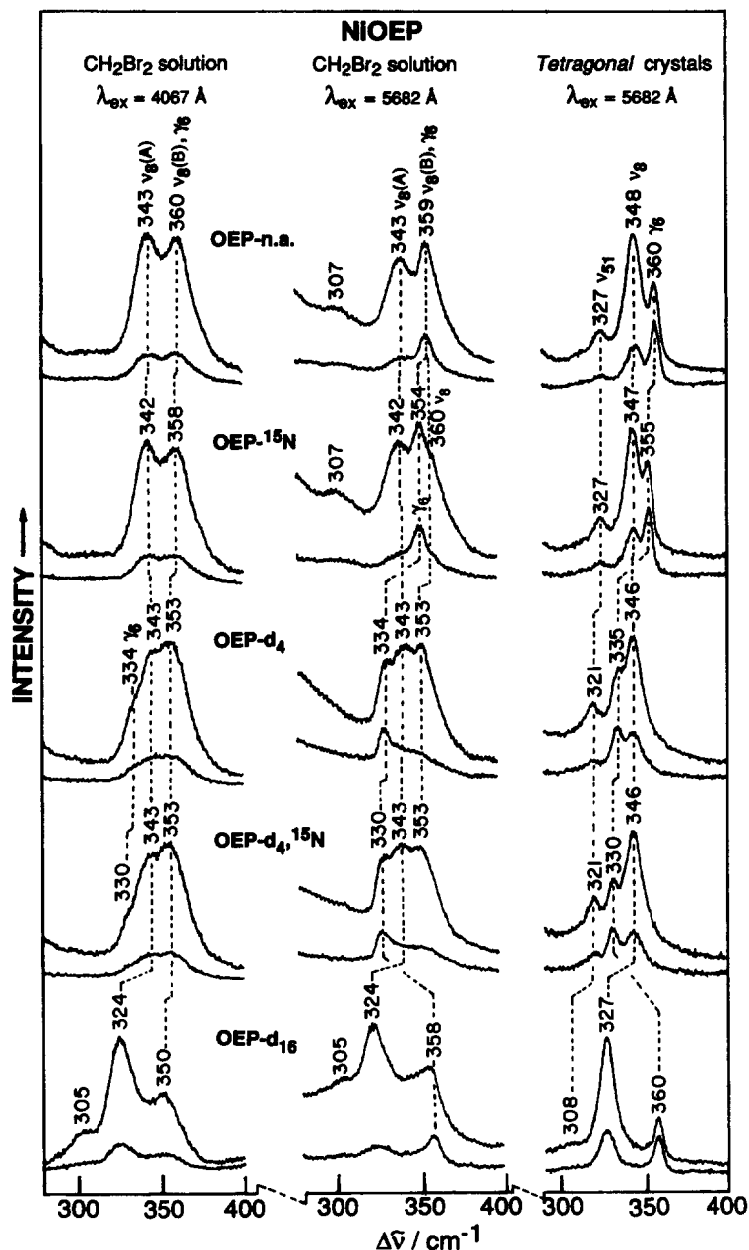
Fig. 12. Solution (in CH_2Br_2, left and middle panels) and tetragonal crystal (in KCl, right panel) RR spectra of NiOEP and its isotopically labelled samples in the 300–400 cm^{-1} region with the indicated excitations. Conditions: backscattering from spinning NMR tube (solution spectra) or from spinning KCl pellet (solid state spectra); 150 mW laser power; 3 cm^{-1} slitwidths; two scans; 1 s integration time at 0.2 cm^{-1} increments. (From ref. 39.)
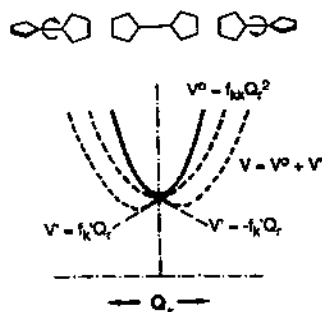
Fig. 13. Conceptual diagram of the softening of a mode Q_r which allows Ni–N (pyrrole) bond to contract by swivelling the pyrrole rings and ruffling the porphyrin. The Ni–N bond extension in the flat structure ($Q_r = 0$) produces a force, f'_k, which lowers the potential by a term V' which is linear for small displacements along Q_r. This flattens the otherwise quadratic potential, V^0, or for sufficiently large f'_k, can lead to a double-minimum potential. (From ref. 39.)

potential for a flat porphyrin, producing a shallow, or even a double-welled potential. This anharmonic potential accords nicely with the analysis by Asher and Murtaugh [40] of the large temperature dependence found for the NiOEP ν_{10} skeletal mode frequency in heated silicone oil and in the gas phase. These authors interpreted this dependence as evidence for anharmonic coupling between ν_{10} and a low frequency mode, the frequency of which they estimated to be 528 ± 150 cm^{-1}, an estimate which is consistent with the γ_{12} frequency. Although Asher and Murtaugh viewed the coupling mode as one leading to porphyrin core expansion, a propeller twisting mode is more plausible, in view of the structural chemistry of NiOEP.

The mode which actually locks NiOEP in the tetragonal crystal structure is probably γ_{14}, calculated [34] at 44 cm^{-1}. Its eigenvector (Fig. 11) also shows a propeller twist, but in addition the methine bridge and substituent atoms are displaced in the same directions as seen in the tetragonal crystal structure. The low frequency of this propeller mode makes it the easiest one along which to distort.

NiOEP solutions probably contain a range of coexisting structures which are more or less ruffled. It can be seen from Fig. 14 that the solution ν_{10} band is broad, much broader than for example for the $[(ImH)_2Fe(III)OEP]^+$ complex or for NiOEP crystals. The ν_{10} frequency is 20 cm^{-1} lower for tetragonal (ruffled) than triclinic (flat) NiOEP crystals, but the difference diminishes at low temperature because of a larger upshift for the former. This upshift is interpreted as evidence of flattening of the porphyrin at low temperature, even within the tetragonal crystal lattice. At elevated temperatures triclinic crystals convert spontaneously to a form containing ruffled NiOEP, consistent with the continuous ν_{10} frequency lowering with increas-
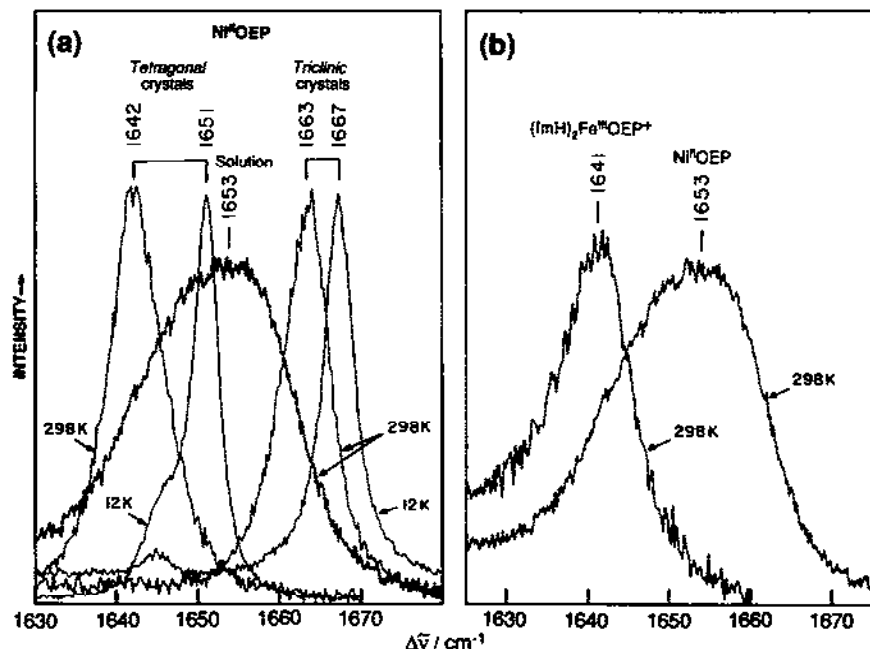
Fig. 14. (a) ν_{10} band shapes in resonance Raman spectra of NiOEP in CH_2Br_2 solution at room temperature (298 K) and in tetragonal and triclinic crystals at room (298 K) and low (12 K) temperatures. (b) Comparison of the ν_{10} RR bands of $(ImH)_2Fe(III)OEP^+$ and NiOEP in CH_2Br_2 solution at room temperature. Conditions: backscattering from spinning NMR tube (solution spectra) or from KCl pellet attached to a cold finger of a CSA-202E closed-cycle liquid helium refrigerator; 5682 Å excitation; 200 mW laser power; 1 cm^{-1} slitwidth; 3 scans; 1 s integration time at 0.2 cm^{-1} increments. (From ref. 39.)

ing temperature observed by Asher and Murtaugh [40]. The higher the temperature the more ruffled the porphyrin. The ν_{10} solution band at room temperature covers the frequency range from tetragonal to triclinic crystals, and is interpreted as containing contributions from a continuous range of structures with varying degrees of ruffling. This distribution can be viewed as resulting from thermal excitation of the soft propeller modes. Independent evidence for coexisting structures comes from observation by Alden et al. [41] that the ν_{10} band shape varies with the excitation wavelength, reflecting different excitation profiles for NiOEP molecules with different degrees of ruffling.

A proper understanding of the NiOEP ν_{10} frequency dependence gains importance in the context of the vibrational frequency shifts to be expected from heating effects in the RR spectroscopy of heme proteins, particularly in studies of phototransients at times (picoseconds) which may be short with respect to the heat dissipation rate in a protein molecule [42(a)]. On the basis

of the NiOEP ν_{10} temperature sensitivity, Asher and Murtaugh [40] warned that large frequency shifts may result from heating effects, and Petrich et al. [42(b)] used the temperature coefficient of this band to interpret the ν_4 frequency shifts of the HbCO picosecond photoproduct as being due to heating, estimating a 218 K rise at 0.9 ps. However, because the NiOEP ν_{10} temperature effect relates to the special dynamic properties of NiOEP, it is not a satisfactory calibrant for heme modes, which are unlikely to show such a large temperature sensitivity.

G. METALLOPORPHYRIN RADICAL CATIONS

One-electron oxidation of the porphyrin ring produces reasonably stable radical cations. These have long been of interest, particularly as models for intermediate states of redox-active heme proteins and of the reaction center of photosynthetic organisms [43]. Their electronic structures have been the subject of much scrutiny and controversy because of the ambiguities created by the near degeneracy of the two HOMOs, a_{1u} and a_{2u} [20]. As illustrated in Fig. 15, the nodal patterns and atomic coefficients are very different for these orbitals, and quite different radical properties can be expected, depending on which orbital contains the unpaired electron. Several physical probes have been applied to these species, including RR spectroscopy [44–48]. Initial results [45] led to some confusion due to artifacts associated with impurities [46], but good-quality spectra are now in hand [44–48].

The RR spectra of copper(II) complexes of OEP and TPP and their radical cations are shown in Fig. 16. The vertical lines indicate the correlation of the normal modes between neutral and radical cation species. These correlations have been secured by determination of isotope shifts, which are essentially unaltered by radical formation. Thus removal of an electron does not significantly change the porphyrin normal-mode compositions. Nevertheless, appreciable frequency shifts are seen for some of the bands, implying changes in the force constants.

The most interesting band is ν_2, which shifts strongly and in opposite directions for CuOEP ($+21$ cm^{-1}) and CuTPP (-32 cm^{-1}). These shifts can be understood on the basis of the HOMO nodal pattern if this orbital is a_{1u} for CuOEP but a_{2u} for CuTTP. The ν_2 mode is mainly $C_\beta C_\beta$ stretching in character (Table 1), and the a_{1u} orbital is antibonding with respect to $C_\beta C_\beta$, while the a_{2u} orbital is bonding. Thus removal of an electron should shift ν_2 up for an a_{1u} radical but down for an a_{2u} radical. TPP radicals have always been considered to be a_{2u} in character [49], but OEP radicals had been thought, on the basis of differing optical spectra, to be either a_{1u} or a_{2u}, depending on the nature of the metal ion and even of the axial ligand [50,51]. The OEP radicals of zinc(II), magnesium(II) and the bromide
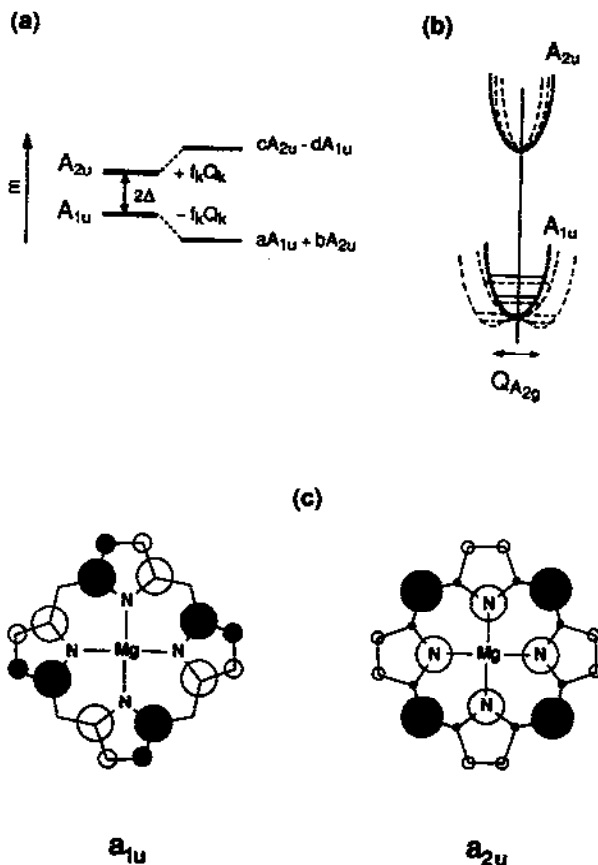
(a)

(b)

(c)

a_{1u} a_{2u}

Fig. 15. Illustration of the pseudo-Jahn–Teller effect. (a) Energy levels of the unperturbed ground (A_{1u}) and excited (A_{2u}) states and of the final states mixed by linear vibronic coupling. (b) Potential curves for the unperturbed (solid lines) and mixed (broken lines) states along an A_{2g} mixing coordinate. Depending on the degree of mixing the lower curve is broadened or converted to a double-minimum potential. (c) The atomic orbital (AO) structure of magnesium porphine in the two highest occupied molecular orbitals, a_{1u} and a_{2u}. The circle sizes are approximately proportional to the AO coefficients [59]: 0.3055 (C_α) and 0.1600 (C_β) for the a_{1u} orbital, and 0.0190 (C_α), 0.0728 (C_β), 04101 (C_m) and 0.2645 (N) for the a_{2u} orbital. The open circles represent negative signs of the upper lobe of the p_π AOs. (From ref. 47.)

complex of cobalt(III) had been classified as a_{1u}, but those of nickel(II), copper(II) and the perchlorate complex of cobalt(III) were classified as a_{2u}.

The RR frequency shift pattern is the same for all these OEP radicals [47,48], however, and differs from those of the TPP radicals [47]. It is therefore evident that the OEP radicals are all a_{1u} in character and that the radical optical spectra are not reliable indicators of the ground state orbital character. Spellane et al. [52] concluded some time ago that the HOMO is
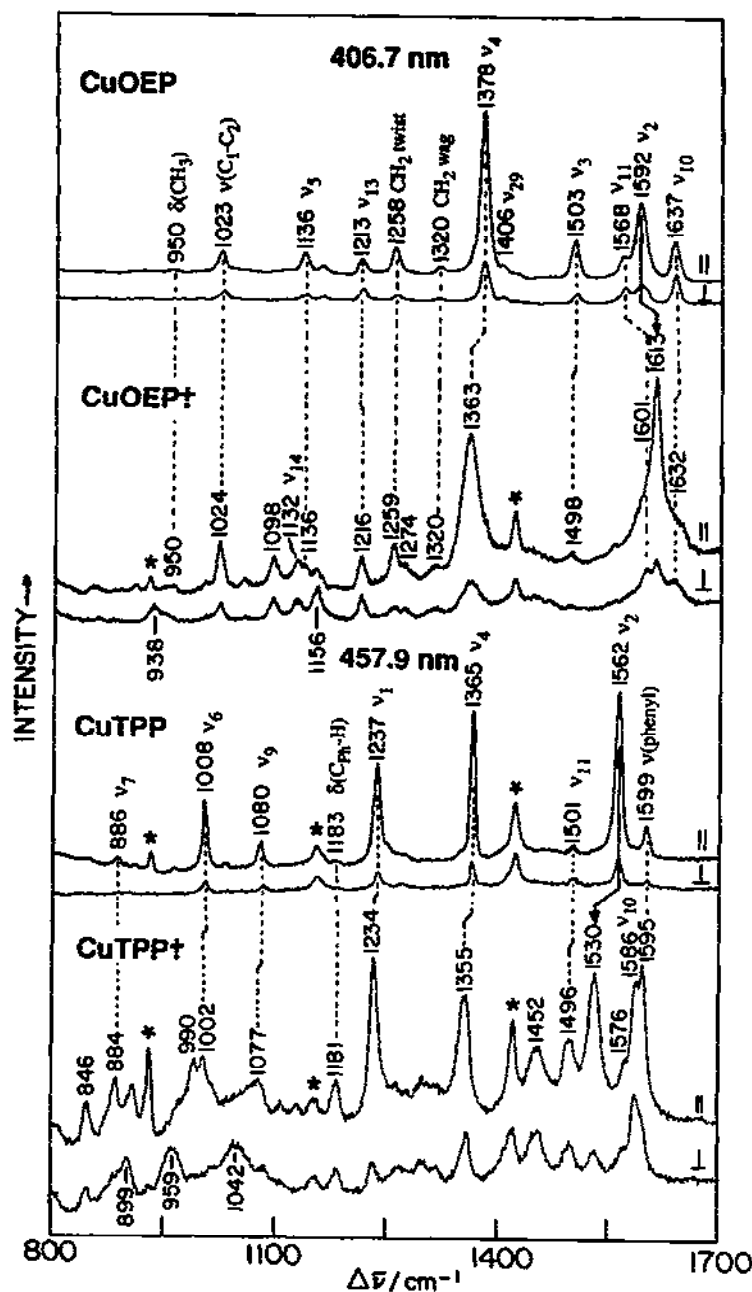
Fig. 16. Comparison of the resonance Raman spectra of CuOEP/CuOEP$^{+\cdot}$ and CuTPP/CuTPP$^{+\cdot}$. Spectra were obtained with 406.7 nm (CuTPP and CuOEP$^{+\cdot}$) and 457.9 nm (CuTPP and CuTPP$^{+\cdot}$) excitation wavelengths, 50 mW laser power, and 8 cm^{-1} slitwidth. The ν_2 upshift for CuOEP$^{+\cdot}$ and downshift for CuTPP$^{+\cdot}$ are indicated with arrows. Asterisks indicate ClO$_4^-$ (electrolyte) and CH$_2$Cl$_2$ solvent bands. (From ref. 47.)
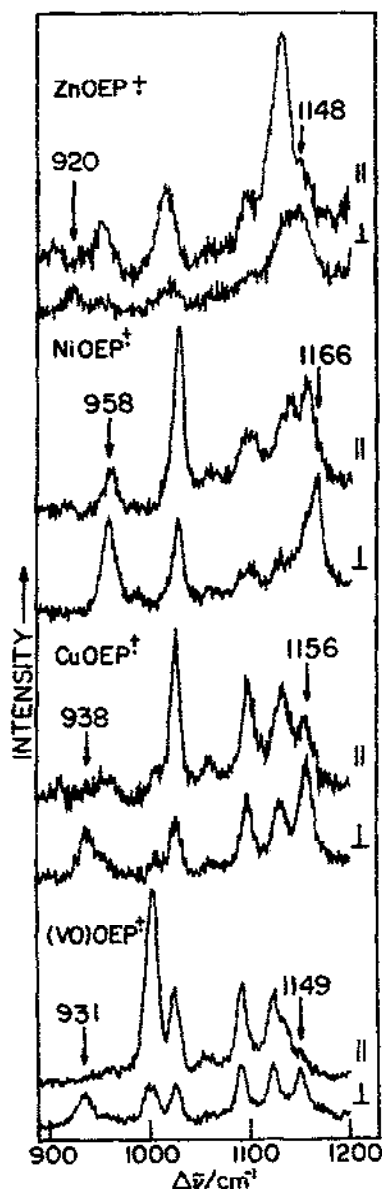
Fig. 17. Anomalously polarized bands in the Soret excited resonance Raman spectra of ZnOEP[+], NiOEP[+], CuOEP[+], and OVOEP[+]. Spectra were obtained with 30–50 mW laser power and 8 cm^{−1} slitwidth using 406.7 nm (Ni, Cu, VO) and 363.8 nm (Zn) excitation wavelengths. (From ref. 47.)

a_{1u} for OEPs but a_{2u} for TPPs from an analysis of the electronic spectra of the neutral porphyrins. The a_{1u} energy is raised by the donor interaction between the ethyl substituents and the porphyrin ring in OEP (see discussion above about hyperconjugation, and Fig. 7), since the C_β atoms have larger a_{1u} than a_{2u} coefficients (Fig. 15). Likewise, the a_{2u} energy is raised by the phenyl–porphyrin interaction in TPP since the a_{2u} orbital has large coefficients at the C_β atoms, where the a_{1u} orbital has nodes.

Since the a_{1u} and a_{2u} orbitals are nearly degenerate, however, the ground and first excited states of the radicals, A_{1u} and A_{2u} or vice versa, are close in energy. They can mix vibronically, producing a pseudo-Jahn–Teller (pJT) effect [47]. The vibrations that can carry out the mixing are of A_{2g} ($= A_{1u} \times A_{2u}$) symmetry; these are the modes which give rise to anomalously polarized RR bands. The pJT effect is expected to flatten the ground state potential (or produce a double-well potential) for the mixing modes, as shown diagramatically in Fig. 15. The radical cation RR spectra do show ap bands in the ca. 1000 cm^{-1} region, as shown in Fig. 17 for OEP radicals; similar bands are seen for TPP radicals [47]. These bands are ring-deuteration sensitive, but they are at much lower frequencies than the deuteration-sensitive ap bands of the neutral porphyrins. This frequency lowering provides direct evidence for the pJT mixing [47].

Since the A_{2g} modes have the symmetry of a molecular rotation, the resulting distortion involves parts of the ring rotating against one another, i.e. alternation of the $C_\alpha C_m$, NC_α or $C_\alpha C_\beta$ bond lengths, or bending of all the $C_m X$ or $C_\beta Y$ substituent bonds in the same direction. A very recent crystal structure of ZnOEP$^{+\cdot}$ shows a clear bond alternation around the 16-membered inner ring, equivalent bonds differing by ca. 0.04 Å [53]. Thus the pJT distortion becomes static in this case, probably frozen in by the strong π–π dimeric interaction observed in the crystal [53].

A number of metalloporphyrin radical crystal structures also reveal a saddle distortion, in which opposite pyrrole rings are alternately displaced up and down relative to the mean porphyrin plane [54]. Figure 18 shows this distortion for (Cl$^-$)Fe(III)TPP$^{+\cdot}$ [55]; the neutral species has a nearly flat porphyrin ring. The saddle distortion corresponds to displacement of the porphyrin along a B_{2u} oop coordinate. The two lowest frequency B_{2u} modes, γ_{17} and γ_{18}, are shown in Fig. 18 as the calculated eigenvectors for NiOEP [34]; a marked resemblance to the observed saddle distortion can be seen. B_{2u} modes are not vibronically active in D_{4h} symmetry. However, if the symmetry is lowered to D_{2d}, then the B_{2u} modes are transformed to A_2, as are the A_{2g} modes, and they can mix the A_{1u} and A_{2u} (now B_1 and B_2) electronic states. The saddle distortion itself leads to D_{2d} symmetry. Consequently, the potential minimum along the low energy B_{2u} coordinates may be displaced from the planar structure owing to electronic effects.
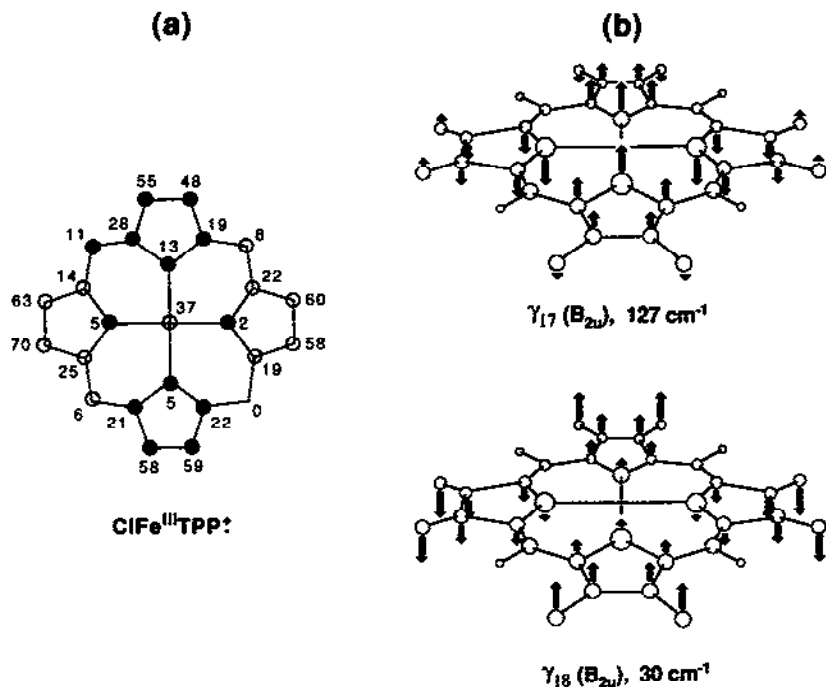
(a) **(b)**

γ_{17} (B$_{2u}$), 127 cm^{-1}

ClFe^{III}TPP$\dagger$

γ_{18} (B$_{2u}$), 30 cm^{-1}

Fig. 18. Illustration of the similarity between the atom displacements (0.01 Å units) for ClFe(III)TPP$^{+\cdot}$ determined by X-ray crystallography [55] (a) and the $B_{2u}(D_{4h}$ symmetry) out-of-plane vibrational modes of NiOEP calculated [34] at 30 cm^{-1} (g_{18}) and 127 cm^{-1} (g_{17}). g_{17} is observed at this frequency in the tetragonal crystalline form of NiOEP [34] (b). (From ref. 47.)

However, Scheidt and Lee [54] expressed the view that the saddle distortion is a solid state effect, resulting from intermolecular interactions. These interactions induce a saddle distortion in order to alleviate steric interference by the phenyl groups of the TPP radicals, which have provided almost all the structural data to date. The recently determined crystal structure of [Cu(TMP)$^+$](SbCl$_6^-$) (TMP = tetramesitylporphyrin) shows non-interacting radicals, and a flat porphyrin ring [56]. Unfortunately, there is no evidence for the extent of the saddle distortion for metalloporphyrin radicals in solution.

H. FUTURE DIRECTIONS

The improved characterization now available for the porphyrin normal modes should permit more penetrating studies of porphyrin structure and dynamics with RR spectroscopy. Heme protein RR spectra are rich in bands, most of which have been characterized only partially if at all.

Interpretation has mostly been at a qualitative level and much more detailed structural information is potentially available. With a good empirical force field in hand it may become possible to model heme protein RR spectra for comparison with experiment and thereby gain insight into the heme–protein interactions. The low frequency modes, which should be especially responsive to the out-of-plane distortions seen in heme protein crystal structures, may repay careful study.

A good deal of attention is currently being focused on the RR spectra of porphyrins with reduced rings [57]: chlorins, bacteriochlorins and isobacteriochlorins, which are widely distributed in nature. A number of systematic studies have been carried out, and detailed assignments are currently in progress. While some correlations with porphyrin modes are apparent in these spectra, exploratory calculations by Boldt et al. [58], using the QCFF/π semiempirical electronic structure program, suggest that considerable localization to fragments of the ring is induced by the reduction of the outer pyrrole bonds. The new porphyrin empirical force field should be helpful in clarifying this issue and in carrying forward structural analysis on these interesting chromophores.

REFERENCES

1 (a) T.G. Spiro (Ed.), Biological Applications of Raman Spectroscopy, Vol. III, Resonance Raman Spectra of Heme and Metalloproteins, Wiley, New York, 1988.
   (b) T. Kitagawa and Y. Ozaki, Struct. Bonding (Berlin), 64 (1987) 71.
   (c) T.G. Spiro, Adv. Protein Chem., 37 (1985) 11.
   (d) T.G. Spiro, in A.B.P. Lever and H.B. Gray (Eds.), Iron Porphyrins, Part II, Addison-Wesley, Reading, MA, 1983, pp. 89–160.
   (e) S.A. Asher, in A. Eiraldo, L.D. Renardi, and E. Cheanconi (Eds.), Methods of Enzymology, Academic Press, New York, 1981, Vol. 76, pp. 371–413.
   (f) R.H. Felton and N.-T. Yu, in D.E. Dolphin (Ed.), The Porphyrins, Vol. III, Part A, Academic Press, New York, 1978, pp. 347–388.
   (g) T. Kitagawa, Y. Ozaki and Y. Kyogoku, Adv. Biophys., 11 (1978) 153.
   (h) A. Warshel, Annu. Rev. Biophys. Bioeng., 6 (1977) 273.
2 (a) T.C. Strekas and T.G. Spiro, Biophys. Biochim. Acta, 263 (1972) 830.
   (b) T.C. Strekas and T.G. Spiro, Biophys. Biochim. Acta, 278 (1972) 188.
3 H. Brunner, A. Mayer and H. Sussner, J. Mol. Biol., 70 (1972) 153.
4 T.G. Spiro and T.C. Strekas, Proc. Natl. Acad. Sci. U.S.A., 69 (1972) 2622.
5 G. Placzek, in E. Marx (Ed.), Handbuch der Radiologie, Akademische Verlagsgesellschaft 6, Leipzig, 1934, Vol. 2, pp. 209–374.
6 T. Yamamoto, G. Palmer, D. Gill, I.T. Salmeen and L. Rimai, J. Biol. Chem., 248 (1973) 5211.
7 (a) T.G. Spiro and T.C. Strekas, J. Am. Chem. Soc., 96 (1974) 338.
   (b) T.G. Spiro and J.M. Burke, J. Am. Chem. Soc., 98 (1976) 5482.
8 L.D. Spaulding, C.C. Cheng, N.-T. Yu and R.H. Felton, J. Am. Chem. Soc., 97 (1975) 2517.
9 T.G. Spiro, J.D. Stong and P. Stein, J. Am. Chem. Soc., 101 (1979) 2648.

10 S. Choi, T.G. Spiro, K.C. Langry, K.M. Smith, L.D. Budd and G.N. LaMar, J. Am. Chem. Soc., 104 (1982) 4345.
11 N. Parthasarathi, C. Hansen, S. Yamaguchi and T.G. Spiro, J. Am. Chem. Soc., 109 (1987) 3865.
12 (a) H. Ogoshi, Y. Saito and K. Nakamoto, J. Chem. Phys., 57 (1972) 4194.
   (b) P. Stein, J.M. Burke and T.G. Spiro, J. Am. Chem. Soc., 97 (1975) 2304.
13 S. Sunder and H. Bernstein, J. Raman Spectrosc., 5 (1976) 351.
14 H. Susi and J.S. Ard, Spectrochim. Acta, Part A, 33 (1977) 561.
15 L.L. Gladkov and K.N. Solovyov, Spectrochim. Acta, Part A, 41 (1985) 1437, 1443.
16 (a) T. Kitagawa, M. Abe and H. Ogoshi, J. Chem. Phys., 69 (1978) 4516.
   (b) M. Abe, T. Kitagawa and Y. Kyogoku, J. Chem. Phys., 69 (1978) 4526.
17 X.-Y. Li, R.S. Czernuszewicz, J.R. Kincaid and T.G. Spiro, J. Phys. Chem., in press.
18 X.-Y. Li, Czernuszewicz, J.R. Kincaid, P. Stein and T.G. Spiro, J. Phys. Chem., in press.
19 T.G. Spiro and X.-Y. Li, Biological Applications of Raman Spectroscopy, Vol. III, Wiley, New York, 1988, Chapter 1.
20 M. Gouterman, in D. Dolphin (Ed.), The Porphyrins, Vol. III, Part A, Academic Press, New York, 1979, pp. 1–156.
21 T.G. Spiro and P. Stein, Annu. Rev. Phys. Chem., 28 (1977) 501.
22 L.D. Cheung, N.-T. Yu and R.H. Felton, Chem. Phys. Lett., 55 (1978) 527.
23 J.R. Kincaid, M.W. Urban, T. Watanabe and K. Nakamoto, J. Phys. Chem., 87 (1983) 3096.
24 (a) A. Desbois, M. Lutz and R. Banarjee, Biochemistry, 18 (1979) 1510.
   (b) A. Desbois and M. Lutz, Biochim. Biophys. Acta, 671 (1981) 168.
25 J.A. Larrabee and T.G. Spiro, J. Am. Chem. Soc., 102 (1980) 4217.
26 S.S. Eaton and G.R. Eaton, J. Am. Chem. Soc., 97 (1975) 3660.
27 (a) G.N. LaMar, G.R. Eaton, R.H. Holm and F.A. Walker, J. Am. Chem. Soc., 95 (1973) 63.
   (b) F.A. Walker, B. Balke and G.A. McDermott, J. Am. Chem. Soc., 104 (1982) 1509.
28 S. Choi, T.G. Spiro, K.C. Langry and K.M. Smith, J. Am. Chem. Soc., 104 (1982) 4337.
29 (a) P.M. Callahan and G.T. Babcock, Biochemistry, 22 (1983) 452.
   (b) J. Van Steelandt-Frentrup, I. Salmeen and G.T. Babcock, J. Am. Chem. Soc., 103 (1981) 5981.
   (c) G.T. Babcock and P.M. Callahan, Biochemistry, 22 (1983) 2314.
30 W.H. Woodruff, R.H. Kessler, N.S. Ferris, R.S. Dallinger, K.R. Carter, T.M. Antalis and G. Palmer, Adv. Chem. Ser., 201 (1982) 625.
31 S. Choi, T.G. Spiro, K.C. Langry, K.M. Smith, L.D. Budd and G.N. LaMar, J. Am. Chem. Soc., 104 (1982) 4345.
32 (a) L. Libit and R. Hoffman, J. Am. Chem. Soc., 96 (1974) 1370.
   (b) M.W. Makinen and A.K. Chung, in A.B.P. Lever and H.B. Gray (Eds.), Iron Porphyrins, Part I, Addison-Wesley, Reading, MA, 1982, pp. 141–219.
33 S. Choi and T.G. Spiro, J. Am. Chem. Soc., 105 (1983) 3683.
34 X.-Y. Li, R.S. Czernuszewicz, J.R. Kincaid and T.G. Spiro, J. Am. Chem. Soc., 111 (1989) 7012.
35 E.F. Meyer, Jr., Acta Crystallogr., Sect. B, B28 (1972) 2162.
36 M.L. Mitchell, X.-Y. Li, J.R. Kincaid and T.G. Spiro, J. Phys. Chem., 91 (1987) 4690.
37 J.L. Hoard, in K.M. Smith (Ed.), Porphyrins and Metalloporphyrins, Elsevier, Amsterdam, 1975, Chapter 8.
38 (a) D.L. Cullen and E.F. Muier, Jr., J. Am. Chem. Soc., 96 (1974) 2095.
   (b) T.D. Brennan, W.R. Scheidt and J.A. Shelnutt, J. Am. Chem. Soc., 110 (1988) 3919.

39 R.S. Czernuszewicz, X.-Y. Li and T.G. Spiro, J. Am. Chem. Soc., 111 (1989) 7021.
40 S.A. Asher and J. Murtaugh, J. Am. Chem. Soc., 105 (1983) 7244.
41 R.G. Alden, B.A. Crawford, M.R. Ondrias and J.A. Shelnutt, J. Am. Chem. Soc., 111 (1989) 2070.
42 (a) E.R. Henry, M. Levitt and W.A. Eaton, Proc. Natl. Acad. Sci., U.S.A., 82 (1985) 2039.
    (b) J.W. Petrich, C. Poyart and J.L. Martin, Biochemistry, 27 (1988) 4049.
43 W.W. Parson and B. Ke, in Grovindijee (Ed.), Photosynthesis: Energy Conversion by Plants and Bacteria, Academic Press, New York, 1983.
44 H. Yamaguchi, M. Nakano and K. Itoh, Chem. Lett., (1982) 1397.
45 D. Kim, L.A. Miller, G. Rakhit and T.G. Spiro, J. Phys. Chem., 90 (1986) 3320.
46 A. Salehi, W.A. Oertling, G.T. Babcock and C.K. Chang, J. Am. Chem. Soc., 108 (1986) 5630.
47 R.S. Czernuszewicz, K.A. Macor, X.-Y. Li, J.R. Kincaid and T.G. Spiro, J. Am. Chem. Soc., 111 (1989) 3860.
48 (a) W.A. Oertling, A. Salehi, Y.C. Chung, G.E. Leroi, C.K. Chang and G.T. Babcock, J. Phys. Chem., 91 (1987) 5887.
    (b) W.A. Oertling, A. Salehi, C.K. Chang and G.T. Babcock, J. Phys. Chem., 93 (1989) 1311.
49 J. Fajer, D.C. Borg, A. Forman, D. Dolphin and R.H. Felton, J. Am. Chem. Soc., 92 (1970) 3451.
50 J. Fajer, D.C. Borg, A. Forman, R.H. Felton, L. Vegh and D. Dolphin, Ann. N.Y. Acad. Sci., 206 (1973) 349.
51 D. Dolphin, Z. Muljiani, K. Rousseau, D.C. Borg, J. Fajer and R.H. Felton, Ann. N.Y. Acad. Sci., 206 (1973) 177.
52 P.J. Spellane, M. Gouterman, A. Antepas, S. Kim and Y.C. Liu, Inorg. Chem., 19 (1980) 386.
53 H. Song, C.A. Reed and W.R. Scheidt, J. Am. Chem. Soc., 111 (1989) 6867.
54 W.R. Scheidt and Y.J. Lee, Struct. Bonding (Berlin), 64 (1987) 1.
55 G. Buisson, A. Deronzier, E. Düee, P. Gans, J.C. Marchon and J.R. Regnard, J. Am. Chem. Soc., 104 (1982) 6793.
56 H. Song, C.A. Reed and W.R. Scheidt, J. Am. Chem. Soc., (1989) in press.
57 G.A. Schick and D.F. Bocian, Biochim. Biophys. Acta, 895 (1987) 127, and references cited therein.
58 N.J. Boldt, R.J. Donohoe, R.R. Birge and D.F. Bocian, J. Am. Chem. Soc., 109 (1987) 2284.
59 D. Spangler, G.M. Maggiora, L.L. Shipman and R.E. Christofferson, J. Am. Chem. Soc., 99 (1977) 7478. The orbital coefficients shown in Fig. 15 were kindly supplied by Dr. James Petke.